Giant magnetic response of a two-dimensional antiferromagnet

Lin Hao[1], D. Meyers[2], Hidemaro Suwa[1,3], Junyi Yang[1], Clayton Frederick[1], Tamene R. Dasa[4],
Gilberto Fabbris[2], Lukas Horak[5], Dominik Kriegner[5,6], Yongseong Choi[7], Jong-Woo Kim[7],
Daniel Haskel[7], Philip J. Ryan[7,8], Haixuan Xu[4]*, Cristian D. Batista[1,9]*, M. P. M. Dean[2]*
and Jian Liu[1]*

A fundamental difference between antiferromagnets and ferromagnets is the lack of linear coupling to a uniform magnetic field due to the staggered order parameter[1]. Such coupling is possible via the Dzyaloshinskii–Moriya (DM) interaction[2,3], but at the expense of reduced antiferromagnetic (AFM) susceptibility due to the canting-induced spin anisotropy[4]. We solve this long-standing problem with a top-down approach that utilizes spin–orbit coupling in the presence of a hidden SU(2) symmetry. We demonstrate giant AFM responses to sub-tesla external fields by exploiting the extremely strong two-dimensional critical fluctuations preserved under a symmetry-invariant exchange anisotropy, which is built into a square lattice artificially synthesized as a superlattice of $SrIrO_3$ and $SrTiO_3$. The observed field-induced logarithmic increase of the ordering temperature enables highly efficient control of the AFM order. Our results demonstrate that symmetry can be exploited in spin–orbit-coupled magnets to develop functional AFM materials for fast and secured spintronic devices[5-9].

Low-dimensional antiferromagnets, exemplified by high-T_c cuprates, are known for extremely rich emergent behaviours, such as unconventional superconductivity, exotic magnetism, magnon condensates, quantum phase transitions and criticality[10-12]. According to the Mermin–Wagner theorem[13], strong critical fluctuations of an isotropic two-dimensional (2D) antiferromagnet prohibit long-range magnetic ordering at finite temperatures, and lead to large magnetic fluctuations and an exponentially diverging magnetic correlation length $\xi \propto e^{2\pi\rho_s/T}$ (where ρ_s is the stiffness) as temperature $T \to 0$[14]. Although it is well known that a magnetic field can suppress the fluctuations and increase the Néel temperature in quasi-2D materials, the induced Zeeman energy must be comparable to the AFM interaction to significantly enhance the ordering stability[15]. As a result, the field required for a sizable or observable effect is often very large, and even unpractical. The underlying limitation originates from the fact that the AFM order is a locked pair of opposite interpenetrating ferromagnetic sublattices[16] (Fig. 1a), and the direct linear coupling between the staggered moment M_s and an external field is symmetrically forbidden. In fact, M_s only responds linearly to a staggered field h_s through $\chi_{AF} = dM_s/dh_s$, where χ_{AF} is the AFM staggered susceptibility.

Despite the lack of direct coupling of the external field to the collinear AFM order parameter (OP), an indirect linear coupling is enabled in the presence of spin canting, which is caused by the antisymmetric anisotropic exchange—the well-known DM interaction[2,3] (Fig. 1b). The canting creates a small net moment and allows the external field to linearly drive the AFM order as an effective staggered field. The DM interaction is, however, also accompanied by a symmetric anisotropic exchange interaction[2]. Both interactions necessarily induce local spin anisotropy[17] (Fig. 1b). This route thus presents a dilemma in that the enforced magnetic axis confines the originally isotropic AFM spins (Fig. 1a) and reduces the value of χ_{AF}.

Although enabling a strong linear coupling and preserving the 2D χ_{AF} seem fundamentally incompatible, we show here that a solution is possible if the spin isotropy is protected by the global symmetry of the system under all local anisotropic exchanges (Fig. 1c). Such a symmetry-invariant exchange anisotropy was first proposed more than two decades ago in the context of superexchange pathways in spin-half AFM square lattices in the absence of direct exchange[17], but, to the best of our knowledge, has not been experimentally realized or utilized. The proposed concept was demonstrated by an effective Hamiltonian including an AFM Heisenberg interaction J, a DM interaction $\mathbf{D}_{ij}$, and a symmetric anisotropic exchange δ as

$$H = \sum_{\langle i,j \rangle} [J\mathbf{S}_i \cdot \mathbf{S}_j + \mathbf{D}_{ij} \cdot \mathbf{S}_i \times \mathbf{S}_j + \delta S_i^z S_j^z] - h \sum_i S_i^x, \quad (1)$$

where $\langle i,j \rangle$ runs over all neighbouring pairs. The last term of equation (1) represents the Zeeman energy in a uniform magnetic field B along the x-axis with $h = g_{aa}\mu_B B$, where $g_{aa} \approx -2$ is the g-factor and μ_B is the Bohr magneton. While the DM and symmetric anisotropic terms usually induce spin anisotropy and suppress the large χ_{AF} of a pure Heisenberg model, it was shown that the continuous SU(2) spin symmetry will be preserved if the DM vectors satisfy the so-called 'unfrustrated condition'[17] $\sum_C \mathbf{D}_{ij} = 0$, where C denotes any closed loop in the 2D lattice plane. This condition is fulfilled, for instance, when the DM vectors $\mathbf{D}_{ij}$ are all perpendicular to the basal plane and alternate their signs (Fig. 1d). As a result, $\delta = \sqrt{J^2 + |\mathbf{D}_{ij}|^2} - J$,

[1]Department of Physics and Astronomy, University of Tennessee, Knoxville, TN, USA. [2]Department of Condensed Matter Physics and Materials Science, Brookhaven National Laboratory, Upton, NY, USA. [3]Department of Physics, University of Tokyo, Tokyo, Japan. [4]Department of Materials Science and Engineering, University of Tennessee, Knoxville, TN, USA. [5]Department of Condensed Matter Physics, Charles University, Prague, Czech Republic. [6]Institute of Physics, Academy of Sciences of the Czech Republic, Prague, Czech Republic. [7]Advanced Photon Source, Argonne National Laboratory, Argonne, IL, USA. [8]School of Physical Sciences, Dublin City University, Dublin, Ireland. [9]Quantum Condensed Matter Division and Shull-Wollan Center, Oak Ridge National Laboratory, Oak Ridge, TN, USA. *e-mail: hxu8@utk.edu; cbatist2@utk.edu; mdean@bnl.gov; jianliu@utk.edu
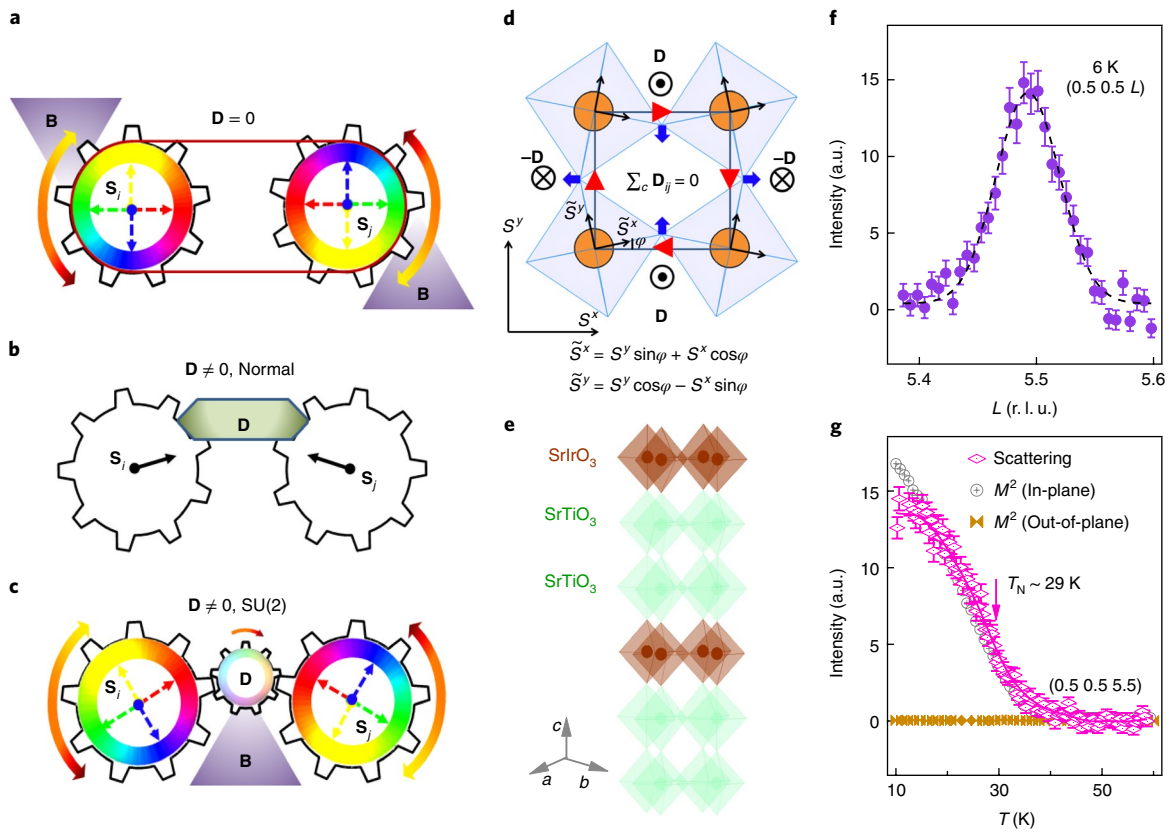
Fig. 1 | Design and realization of spin canting without spin anisotropy via a SU(2)-invariant DM interaction. a–c, Schematic diagrams of a pair of antiferromagnetically coupled spins. The pair is fully antiparallel and free to rotate together in all directions (**a**). Under a typical DM interaction (**b**), the pair is canted towards a preferential orientation, which is stable against magnetic fields. If the DM interaction preserves the rotational symmetry (**c**), the pair is again highly susceptible to magnetic fields via the canting. **d**, A square lattice where DM interactions caused by planar octahedral rotation (blue arrows) preserves SU(2) symmetry. The spins S can be mapped on a local spin frame $\widetilde{S}$ according to the shown transformation. Red arrows denote the summation loop of DM vectors. **e**, Layered structure of the superlattice. **f**, Reciprocal space L-scan across the (0.5 0.5 5.5) magnetic reflection at the Ir L_3-edge and 6 K. **g**, Temperature dependence of the AFM Bragg peak intensity at zero field reveals $T_N \sim 29$ K, defined as the maximum slope of the AFM OP. A similar onset behaviour is seen in the in-plane remnant magnetization, which is plotted squared since scattering is proportional to the OP squared[30]. The out-of-plane component was also shown for comparison. The error bars indicate the statistical error.

and equation (1) acquires a hidden SU(2) symmetry which can be unveiled by a staggered z-axis rotation of the local spin reference frame by the canting angle φ ($\tan(2\varphi) = D/J$, with $D = |\mathbf{D}_{ij}|$)[17] (Fig. 1d). In the new frame, equation (1) recovers an isotropic 2D Heisenberg model with a large χ_{AF} (Methods)

$$H = \sum_{\langle i,j \rangle} \widetilde{J} \; \widetilde{\mathbf{S}}_i \cdot \widetilde{\mathbf{S}}_j - h\cos\varphi \sum_i \widetilde{S}_i^x + h\sin\varphi \sum_i e^{i\mathbf{Q}\cdot\mathbf{r}_i}\widetilde{S}_i^y \quad (2)$$

Here $\widetilde{J} = \sqrt{J^2 + D^2}$, and $\mathbf{Q} = (\pi, \pi)$ is the AFM ordering wave-vector. Fundamentally, this condition is achieved here because the global structural point group symmetry of the square lattice is preserved by the in-plane octahedral rotations that create the anisotropic exchange. It is noteworthy that the hidden SU(2) symmetry holds not only in the effective spin model, but also the high-energy single-band Hubbard model including the charge degrees of freedom[17]. The SU(2)-invariant exchange anisotropy is remarkable in that the large χ_{AF} is not only preserved but also manifests under $h \ll J$ due to the linear coupling with the AFM OP $\widetilde{M}_{st} = \sum_i e^{i\mathbf{Q}\cdot\mathbf{r}_i}\widetilde{S}_i^y$ unveiled in equation (2). A key to this mechanism is a large DM interaction, since the linear coupling scales with the canting angle φ.

To exploit the response of the hidden SU(2) symmetry to the external field, we employ the epitaxial superlattices of $(SrIrO_3)_1$/

$(SrTiO_3)_2$ grown along the pseudocubic [001]-direction on $SrTiO_3$ substrates[18] (Fig. 1e). The design utilizes the magnetic degrees of freedom arising from Kramers doublets of the Ir^{4+} $5d^5$ ions[19–22]. As found in a variety of iridate compounds[10,20,23], these doublets result from the splitting of the active t_{2g} levels caused by a large spin–orbit coupling ~0.4 eV and can be represented with effective $S = 1/2$ pseudospins (Supplementary Information 3). In this situation, even a weak Coulomb repulsion is sufficient to generate a 2D AFM Mott insulating state, such as that in Sr_2IrO_4 (ref. [23]). On the other hand, unlike ordinary $S = 1/2$ spins present in lighter transition metal oxides, the effective $S = 1/2$ pseudospins have far stronger spin–orbit coupling, which leads to the much larger DM interactions and spin canting commonly found in magnetic iridates[19,24,25]. Indeed, the ground state of the confined IrO_6 octahedral layer in our superlattice is revealed as a 2D antiferromagnet with a Néel transition at $T_N \sim 29$ K and significant canted moments (Fig. 1f,g), which is essential for the hidden SU(2) symmetry. The reason for using a bilayer $SrTiO_3$ spacer here is twofold. Firstly, to realize the unfrustrated condition, we performed density functional theory calculations and found only the in-plane octahedral rotation exists, whereas out-of-plane rotation would occur when the spacer is thinner (Supplementary Information 1). We confirm this D_4-symmetric structure by synchrotron X-ray diffraction (Supplementary Information 2), fulfilling the unfrustrated condition. Such an
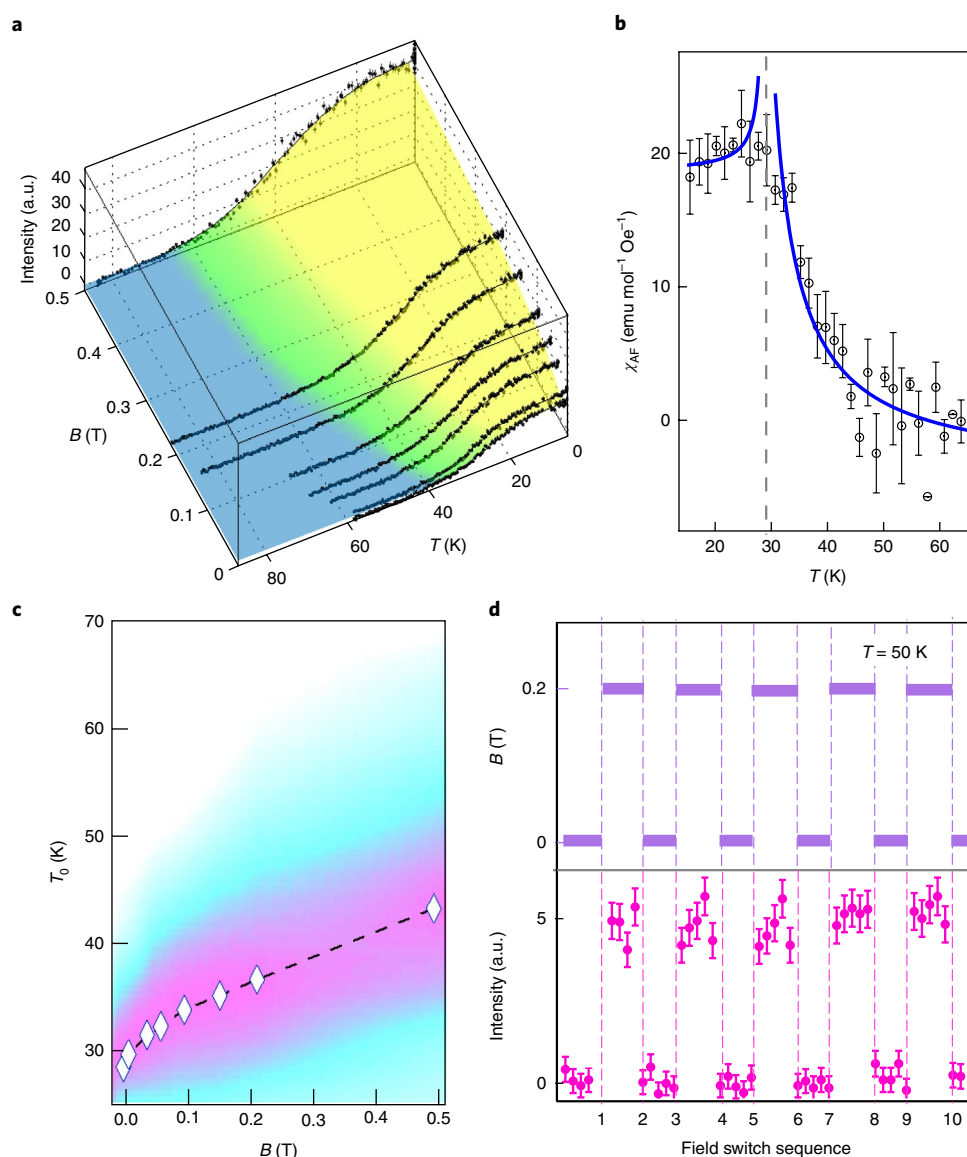
Fig. 2 | Magnetic diffraction in applied magnetic fields. a, Temperature dependence of the (0.5 0.5 5.5) AFM Bragg peak under various in-plane magnetic fields. The coloured surface mesh highlights the dramatic increase of the temperature boundary below which the magnetic peak becomes observable. **b**, Temperature-dependent χ_{AF} extracted from **a**. The magnitude was calibrated by assuming a constant spin canting angle $\varphi \sim 8°$. The error bar represents the standard deviation from the average value during the data-binding process. Lines are drawn to guide the eye. **c**, Relation between crossover temperature T_0 and magnetic field B. The colour scale highlights the crossover region. **d**, The magnetic peak intensity in response to an on/off 0.2 T field-switching sequence at 50 K. The error bars represent the statistical error.

octahedral rotation pattern is also consistent with the observed in-plane canted moment, similar to Sr_2IrO_4 with a canting angle $\varphi \sim 10°$ (refs [19,26]), and the absence of out-of-plane net magnetization (Fig. 1g). Other layered perovskites such as La_2CuO_4 tend to have out-of-plane octahedral rotations[17]. Furthermore, increasing the interlayer spacing reduces the interlayer exchange $J_\perp$. This is crucial because $J_\perp$ stabilizes T_N at the cost of reducing χ_{AF} (ref. [27]) and it must be orders of magnitude smaller than h in order to exploit the symmetry-invariant exchange anisotropy of a quasi-2D system. Indeed, when decreasing the $SrTiO_3$ spacer from a bi-layer to a single-layer, T_N is increased from ~29 K (Fig. 1g) to ~140 K (refs [18,28]), consistent with a strong increase of $J_\perp$.

Having verified the realization of the hidden SU(2) symmetry, we explored the responses of the AFM order and transition to an in-plane magnetic field. Figure 2a shows the temperature dependences of the AFM Bragg peak intensity under various magnetic fields.

The value of χ_{AF}, which is defined at the zero-field limit, is extracted from low-field data (Methods) and clearly shows a divergent behaviour in Fig. 2b around T_N. Moreover, compared to cuprates[29], it shows an enhancement of about two orders of magnitude, manifesting giant 2D AFM fluctuations. As the field further increases from 0 to 0.5 T, one can see from Fig. 2a that the thermal stability of the AFM order is rapidly enhanced. For instance, while the AFM Bragg peak onsets at ~40 K at zero field, it is readily observable below 70 K at just 0.5 T. Since the zero-field Néel transition becomes a crossover under an external field due to the linear coupling, the crossover temperature, T_0, is defined similarly to T_N as the temperature that maximizes the slope of the OP extracted from the peak intensity[30]. Figure 2c shows the drastic enhancement of T_0, especially at small fields near 0.1 T, displaying a logarithmic behaviour (Fig. 3a). The enhancement of T_0 at 0.5 T is ~50%, which is remarkable considering that the Zeeman energy at this maximum applied field is
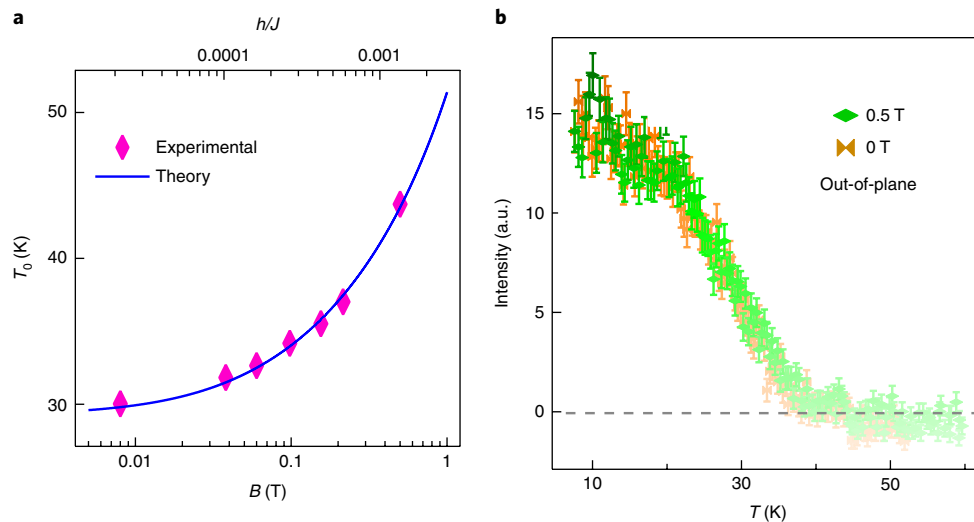
Fig. 3 | Theoretical analysis and experimental confirmation. a, Comparison between the measured field-dependence of the crossover temperature T_0 and the logarithmic increase [equation (3)] expected for a quasi-2D version of equation (1). J is set as 50 meV (refs [20,31,32]) to normalize h (Methods). **b**, Temperature scan of the (0.5 0.5 5.5) magnetic peak under a 0.5 T out-of-plane ($B//z$) field is shown together with a zero-field scan done under the same conditions. The error bars represent the statistical error.

still three orders of magnitude smaller than $J\sim50$ meV (refs [20,31,32]) (Fig. 3a). The extreme sensitivity of T_0 enables complete on/off switching of the AFM order with small magnetic fields. Figure 2d shows the in-situ observation of the AFM Bragg peak at 50 K. Zero counts are observed when the field is off because there is no AFM order at this temperature. In contrast, a clear magnetic peak intensity is detected when the field is on, indicating activation of the AFM long-range order. The switching is highly reliable, as evidenced from the reproducible and prompt response of the peak intensity even after turning the magnetic field on and off multiple times. Although this measurement does not resolve the switching dynamics, due to the lack of ultrafast time resolution, it will be an interesting direction for future investigation because the strong exchange interaction is expected to afford a rapid response[7,9] which can now be triggered by a small external field under the symmetry-invariant exchange anisotropy.

The rapid increase of $T_0(B)$ can be quantitatively accounted for by equation (2) with addition of the small higher-order exchange anisotropies, $H' = -\Gamma_1 \sum_{\langle i,j \rangle} \tilde{S}_i^z \tilde{S}_j^z$, induced by the small Hund's coupling of the Ir^{4+} ion[19,20]. This term is responsible for easy-plane anisotropy and is $\sim10^{-4}J$ (Methods). Although the Hamiltonian $(H+H')$ lowers the SU(2) symmetry towards U(1), the resulting planar continuous symmetry still leads to an exponentially divergent antiferromagnetic correlation length in the vicinity of a Berezinskii–Kosterlitz–Thouless (BKT) transition[33]: $\xi \sim e^{b/\sqrt{t}}$, where $t = \frac{T - T_{BKT}}{T_{BKT}}$ and b is a Γ_1-dependent constant. This essential singularity of the transition point renders the AFM order highly susceptible to the external field. We then treat h and $J_\perp$ as perturbations to $(H+H')$. These perturbations are negligible in the $T \gg T_0$ regime dominated by in-plane vortex–antivortex excitations. The crossover to the regime characterized by a large AFM OP occurs at the temperature scale T_0, where the combined cost from h and $J_\perp$ for separating an in-plane vortex–antivortex pair by a distance ξ is comparable to the intralayer exchange energy[33]: $(2\,|J_\perp|\,S^2 + S\,|h\sin\varphi|)\xi^2 \sim J\,S^2\ln\xi$. The resulting crossover temperature is

$$T_0 = T_{BKT} + \frac{4b^2 T_{BKT}}{\left[\ln\left(\frac{c\tilde{J}S^2}{2\,|J_\perp|\,S^2 + S\,|h\sin\varphi|}\right)\right]^2} \quad (3)$$

where c is a constant accounting for the effects of quantum fluctuations and disorder. At zero field, the finite $J_\perp$ turns the BKT transition into a Néel transition—that is, $T_N = T_0(h=0)$. The rapid increase of T_0 arises from the logarithmic dependence on the magnetic field, which linearly couples to the AFM order. The prerequisite is that the effective staggered field $|h\sin\varphi|$ must be larger than $J_\perp$. To fit the observed $T_0(B)$ with equation (3), we estimated the constant b from the crossover temperature calculated with classical Monte Carlo simulations (Methods). Figure 3a shows that the experimental data is well explained by equation (3). The estimated $J_\perp \sim 10^{-3}$ meV is two orders smaller than the Zeeman energy at 0.5 T.

In the absence of the DM interaction, the linear field–OP coupling in equation (3) would have to be replaced by the much weaker quadratic coupling that gives an energy contribution two orders of magnitude smaller than the interlayer interaction for a 0.5 T field—that is, to a negligibly small field-induced increase of T_0 (Methods). We confirmed this picture by applying a 0.5 T out-of-plane field ($B//z$) that has no coupling to the in-plane spin canting. The measured temperature dependence of the magnetic Bragg peak indeed shows no observable change of T_0 compared with T_N (Fig. 3b). As a comparison, similarly small effects have been seen in Cu^{2+}-based quasi-2D materials with a canted moment that is two orders smaller than iridates, and a significant increase of T_0/T_N therein demands a much larger field to match the AFM exchange[15].

Our study shows that a SU(2)-invariant DM interaction can enable an unprecedented control of AFM order by a small magnetic field. This mechanism drives a logarithmic increase of the ordering temperature of a 2D antiferromagnet by exploiting the large 2D critical fluctuations under a hidden continuous symmetry. Engaging with the hidden SU(2) symmetry may lead to dramatic effects, pointing to rich spin–orbit physics of iridates beyond the high-T_c analogy. Since symmetry-invariant exchange anisotropy is not restricted to square lattices, the demonstration of this concept is expected to facilitate development of new antiferroic systems and devices with improved efficiency.

Methods

Methods, including statements of data availability and any associated accession codes and references, are available at https://doi.org/10.1038/s41567-018-0152-6.

References

1. Néel, L. in *Nobel Lectures, Physics, 1963–1970* 318–341 (Elsevier, Amsterdam, 1972).
2. Moriya, T. Anisotropic superexchange interaction and weak ferromagnetism. *Phys. Rev.* **120**, 91–98 (1960).
3. Dzyaloshinsky, I. A thermodynamic theory of 'weak' ferromagnetism of antiferromagnetics. *J. Phys. Chem. Solids* **4**, 241–255 (1958).
4. Ren, Y. et al. Temperature-induced magnetization reversal in a YVO₃ single crystal. *Nature* **396**, 441–444 (1998).
5. Železný, J. et al. Relativistic Néel-order fields induced by electrical current in antiferromagnets. *Phys. Rev. Lett.* **113**, 157201 (2014).
6. Marti, X. et al. Room-temperature antiferromagnetic memory resistor. *Nat. Mater.* **13**, 367–374 (2014).
7. Kimel, A. V., Kirilyuk, A., Tsvetkov, A., Pisarev, R. V. & Rasing, T. Laser-induced ultrafast spin reorientation in the antiferromagnet TmFeO₃. *Nature* **429**, 850–853 (2004).
8. Wadley, P. et al. Electrical switching of an antiferromagnet. *Science* **351**, 587–590 (2016).
9. Šmejkal, L., Mokrousov, Y., Yan, B. & MacDonald, A. H. Topological antiferromagnetic spintronics. *Nat. Phys.* **14**, 242–251 (2018).
10. Rau, J. G., Lee, E. K.-H. & Kee, H.-Y. Spin–orbit physics giving rise to novel phases in correlated systems: Iridates and related materials. *Annu. Rev. Condens. Matter Phys.* **7**, 195–221 (2016).
11. Basov, D. N., Averitt, R. D., & Hsieh, D. Towards properties on demand in quantum materials. *Nat. Mater.* **16**, 1077–1088 (2017).
12. Keimer, B. & Moore, J. E. The physics of quantum materials. *Nat. Phys.* **13**, 1045–1055 (2017).
13. Mermin, N. D. & Wagner, H. Absence of ferromagnetism or antiferromagnetism in one- or two-dimensional isotropic Heisenberg models. *Phys. Rev. Lett.* **17**, 1133–1136 (1966).
14. Chakravarty, S., Halperin, B. I. & Nelson, D. R. Two-dimensional quantum Heisenberg antiferromagnet at low temperatures. *Phys. Rev. B* **39**, 2344–2371 (1989).
15. Povarov, K. Y., Smirnov, A. I. & Landee, C. P. Switching of anisotropy and phase diagram of the Heisenberg square-lattice $S = 1/2$ antiferromagnet Cu(pz)₂(ClO₄)₂. *Phys. Rev. B* **87**, 214402 (2013).
16. Wadhawan, V. *Introduction to Ferroic Materials* (Gordon and Breach, Amsterdam, 2000).
17. Shekhtman, L., Entin-Wohlman, O. SpringerAmpamp; Aharony, A. Moriya's anisotropic superexchange interaction, frustration, and Dzyaloshinsky's weak ferromagnetism. *Phys. Rev. Lett.* **69**, 836–839 (1992).
18. Hao, L. et al. Two-dimensional $J_{eff} = 1/2$ antiferromagnetic insulator unraveled from interlayer exchange coupling in artificial perovskite iridate superlattices. *Phys. Rev. Lett.* **119**, 027204 (2017).
19. Jackeli, G. & Khaliullin, G. Mott insulators in the strong spin–orbit coupling limit: From Heisenberg to a quantum compass and Kitaev models. *Phys. Rev. Lett.* **102**, 017205 (2009).
20. Katukuri, V. M. et al. Mechanism of basal-plane antiferromagnetism in the spin–orbit driven iridate Ba₂IrO₄. *Phys. Rev. X* **4**, 021051 (2014).
21. Bogdanov, N. A. et al. Orbital reconstruction in nonpolar tetravalent transition-metal oxide layers. *Nat. Commun.* **6**, 7306 (2015).
22. Solovyev, I. V., Mazurenko, V. V. & Katanin, A. A. Validity and limitations of the superexchange model for the magnetic properties of Sr₂IrO₄ and Ba₂IrO₄ mediated by the strong spin–orbit coupling. *Phys. Rev. B* **92**, 235109 (2015).
23. Kim, B. J. et al. Phase-sensitive observation of a spin–orbital Mott state in Sr₂IrO₄. *Science* **323**, 1329–1332 (2009).
24. Kim, J. W. et al. Dimensionality driven spin-flop transition in layered iridates. *Phys. Rev. Lett.* **109**, 037204 (2012).
25. Boseggia, S. et al. Robustness of basal-plane antiferromagnetic order and the $J_{eff} = 1/2$ state in single-layer iridate spin–orbit Mott insulators. *Phys. Rev. Lett.* **110**, 117207 (2013).
26. Wang, F. & Senthil, T. Twisted Hubbard model for Sr₂IrO₄: Magnetism and possible high temperature superconductivity. *Phys. Rev. Lett.* **106**, 136402 (2011).
27. Dean, M. P. M. et al. Spin excitations in a single La₂CuO₄ layer. *Nat. Mater.* **11**, 850–854 (2012).
28. Matsuno, J. et al. Engineering a spin–orbital magnetic insulator by tailoring superlattices. *Phys. Rev. Lett.* **114**, 247209 (2015).
29. Hayden, S. M. et al. Comparison of the high-frequency magnetic fluctuations in insulating and superconducting La₂₋ₓSrₓCuO₄. *Phys. Rev. Lett.* **76**, 1344–1347 (1996).
30. Stöhr, J. & Siegmann, H. C. *Magnetism: From Fundamentals to Nanoscale Dynamics* (Springer, New York, NY, 2006).
31. Kim, J. et al. Magnetic excitation spectra of Sr₂IrO₄ probed by resonant inelastic X-ray scattering: Establishing links to cuprate superconductors. *Phys. Rev. Lett.* **108**, 177003 (2012).
32. Meyers, D. et al. Magnetism in artificial Ruddlesden–Popper iridates leveraged by structural distortions. Preprint at https://arxiv.org/abs/1707.08910 (2017).
33. Hikami, S. & Tsuneto, T. Phase transition of quasi-two dimensional planar system. *Progress. Theor. Phys.* **63**, 387–401 (1980).

Acknowledgements

Author contributions

C.D.B., M.P.M.D. and J.L. conceived and directed the study. L.H., D.M., J.Y. and C.F. undertook sample growth and characterization. L.H., D.M., J.Y., J.W.K. and P.J.R. performed magnetic scattering measurements. L.H., D.M., G.F., Y.S.C. and D.H. conducted XMCD measurements. L.H., D.M., J.Y., L.H. and D.K. collected synchrotron XRD data. L.H. and J.L. analysed data. H.S. and C.D.B. performed Monte Carlo simulations. T.R.D. and H.X. performed first-principles calculations. L.H., H.S., C.D.B., M.P.M.D. and J.L. wrote the manuscript.

Competing interests

The authors declare no competing interests.

Additional information

Methods

First-principles density functional calculations. Density functional theory (DFT) calculations were performed using projector-augmented wave method with the generalized gradient approximation (GGA)[34] as implemented in the Vienna ab-initio Simulation Package[35]. The plane wave cutoff was chosen as 500 eV on the basis of the convergence tests. To model the epitaxial relationship of samples grown on a SrTiO$_3$ substrate, the in-plane lattice parameters were fixed to the substrate value, 3.905 Å. A $4 \times 4 \times 3$ Monkhorst–Pack k-point mesh was used for reciprocal space integrations. Correlation effects were treated by including a Hubbard correction with $U = 2.2$ (5.0) eV and $J = 0.2$ (0.64) eV for Ir (Ti)[36].

Sample growth. The superlattice was deposited on a (001)-oriented SrTiO$_3$ single-crystal substrate using pulsed laser deposition, with a KrF (248 nm) excimer laser. Before deposition, the substrate was pretreated to have a TiO$_2$ termination. The substrate temperature and oxygen pressure were optimized to 700 °C and 0.1 mbar, respectively. Equipped with a reflection high-energy electron diffraction unit, the growth process was in-situ monitored to control the stacking sequence with atomic precision. The details of the growth and sample characterization can be found elsewhere[18].

Experimental investigation of octahedral rotation pattern. Here, we use Glazer's notation for describing octahedral rotation patterns. Following Glazer's arguments, the unit cell of a perovskite material can be enlarged by octahedral rotations, octahedral distortions and cation displacement[37,38]. To distinguish different rotation patterns, Glazer used superscript $+$ ($-$) to denote an in-phase (out-of-phase) rotation of adjacent octahedra along a high-symmetry axis of the pseudocubic cell, and 0 to represent the absence of octahedral rotation. Meanwhile, different rotation amplitudes along various axes are indicated by different letters[37]. For instance, Glazer notation $a^-a^-c^0$ represents a distorted lattice structure with out-of-phase octahedral rotations of the same amplitude along the a and b axes but no octahedral rotation along the c axis (Supplementary Fig. 1a). Similarly, $a^0a^0c^-$ denotes the presence of only an out-of-phase octahedral rotation along the c-axis (Supplementary Fig. 1b). From the side views, one can see that the two types of octahedral rotation patterns lead to very different movements of the planar and apical oxygen ions. Specifically speaking, the planar oxygen ions move away from the ab plane and the apical oxygen ions move away from the c axis under $a^-a^-c^0$, buckling the vertical bond. In contrast, the planar oxygen ions stay within the ab plane and the vertical bond remains straight under $a^0a^0c^-$. The two types of motions may superimpose to create a pattern of $a^-a^-c^-$.

The enlargement of the crystal lattice due to octahedral rotations can be followed by the emergence of half-order Bragg peaks in an X-ray diffraction (XRD) pattern, and the peak intensities are proportional to the octahedral rotation amplitude squared[37,39]. Therefore, from the intensity of specific superlattice peaks, one can identify the lattice distortion due to octahedral rotation. The correspondence of superlattice peaks and octahedral rotation has been thoroughly discussed in refs [37,39]. To access the weak superstructure due to octahedral rotation, we studied the lattice structure with the synchrotron X-ray source at the 33BM beamline at the Advanced Photon Source of Argonne National Laboratory. A unit cell of $a \times a \times 3c$ (a and c are the pseudocubic in-plane and out-of-plane lattice parameters, respectively) was used to define the reciprocal space notation.

Magnetization measurements. Temperature-dependent in-plane and out-of-plane remnant magnetizations were measured with a quantum-design superconducting quantum interference device (SQUID) magnetometer.

X-ray absorption (XAS) and magnetic circular dichroism (XMCD) measurements. To check the robustness of the $J_{\mathrm{eff}} = 1/2$ model in the present superlattice, we performed XAS and XMCD measurements around the Ir L_3- and L_2-edges at beamline 4ID-D of the Advanced Photon Source, Argonne National Laboratory.

Magnetic scattering study. Resonant magnetic X-ray scattering measurements were performed around the Ir L_3-edge at 6IDB beamline at the Advanced Photon Source of Argonne National Laboratory. During the scattering process, a linearly polarized X-ray beam was scattered by both charge and magnetic moments. While the former arises due to non-resonant Thomson scattering, the magnetic scattering intensity can be amplified by choosing an X-ray energy which resonates with the active orbital through atomic transitions. In addition, a charge scattered X-ray has the same polarization as the incident X-ray (σ-σ channel), while the polarization will be rotated 90° by magnetic scattering (σ-π channel). To separate the magnetic contribution from the charge contribution, a polarization analyser was utilized. This method enables the direct detection of the antiferromagnetic order in a thin epitaxial superlattice less than 50 nm thick, which would be impossible by other techniques. The present magnetic scattering experiment is also able to directly probe the staggered moment M_s by measuring the AFM Bragg peak intensity. Because the staggered susceptibility is defined as $\chi_{\mathrm{AF}} = \mathrm{d}M_s/\mathrm{d}h_s$ (h_s is the staggered field) at the zero-field limit ($h_s \to 0$), we extracted the temperature dependence of χ_{AF} at the low-field limit by the relative change of the AFM Bragg peak intensity from zero field to 80 Oe, the smallest field in the current experiment—that is, $\chi_{\mathrm{AF}} \propto \frac{[\sqrt{I(80\ \mathrm{Oe})} - \sqrt{I(0\ \mathrm{Oe})}]}{\sin\varphi \times 80\ \mathrm{Oe}}$. To convert the intensity variation to the change of M_s

and estimate the absolute value of χ_{AP}, the data were further normalized with the remnant magnetization (Fig. 1g) by assuming a constant spin canting angle φ of 8°.

Frame transformation and proof of the hidden SU(2) symmetry. Performing the second-order perturbation calculation to the one-band Hubbard model with the spin-orbit coupling (λ), we obtain an effective spin Hamiltonian

$$H = \sum_{\langle i,j \rangle} [J\mathbf{S}_i \cdot \mathbf{S}_j + \mathbf{D}_{ij} \cdot \mathbf{S}_i \times \mathbf{S}_j + \delta S_i^z S_j^z], \tag{4}$$

where $\mathbf{S}_i$ represents the spin operator at the ith site, $\mathbf{D}_{ij}$ is the DM vector perpendicular to the plane whose absolute value is $D = |\mathbf{D}_{ij}| \propto \lambda$, and $\delta = \sqrt{J^2 + D^2} - J \propto \lambda^2$ is the symmetric exchange anisotropy[17], and the sum runs over all bonds of the square lattice. To unveil the hidden SU(2) symmetry, we change the local reference frame in each of the two sublattices. The new reference frame in sublattice A (B) is obtained by rotating the original reference fame by an angle φ ($-\varphi$) around the z axis (Fig. 1d). The spin operators in the new reference frame become

$$\tilde{S}_A^x = S_A^x \cos\varphi - S_A^y \sin\varphi$$

$$\tilde{S}_A^y = S_A^x \sin\varphi + S_A^y \cos\varphi$$

for any site in sublattice A and

$$\tilde{S}_B^x = S_B^x \cos\varphi + S_B^y \sin\varphi$$

$$\tilde{S}_B^y = -S_B^x \sin\varphi + S_B^y \cos\varphi$$

for any site on sublattice B. The z components remain unchanged. Given that

$$\tilde{\mathbf{S}}_A \cdot \tilde{\mathbf{S}}_B = \cos(2\varphi)\mathbf{S}_A \cdot \mathbf{S}_B + \sin(2\varphi)\hat{\mathbf{z}} \cdot \mathbf{S}_A \times \mathbf{S}_B + [1 - \cos(2\varphi)] S_A^z S_B^z$$

we can rewrite equation (4) as

$$H = \sum_{\langle i,j \rangle} \tilde{J}\tilde{\mathbf{S}}_i \cdot \tilde{\mathbf{S}}_j$$

with $\tilde{J} = \sqrt{J^2 + D^2}$ and $\tan(2\varphi) = D/J$, if the DM vectors satisfy the condition $\sum_C \mathbf{D}_{ij} = 0$, where C denotes any closed directed path consisting of bonds of the square lattice[17]. This condition arises from the fact that the bonds alternate between $A \to B$ and $B \to A$ when we circulate around a closed loop and $\mathbf{D}_{AB} = -\mathbf{D}_{BA}$. The isotropic interaction in the new reference frame reveals that the system has a hidden SU(2) symmetry. The DM vectors of a 2D corner-sharing IrO$_6$ octahedral network with only in-plane octahedral rotation clearly satisfy this condition, as shown in Fig. 1d.

In addition to the superlattices, such a 2D layer also exists in bulk Sr$_2$IrO$_4$, where the condition of the hidden SU(2) symmetry should be satisfied as well[19,26]. However, this material also possesses a relatively large interlayer coupling[40,41], which is fixed by the bulk structure and can not be tuned, masking the 2D critical fluctuations. Furthermore, due to the interlayer coupling, the in-plane canting moments of the different layers within the unit cell adopt a '$+ - - +$' sign pattern along the c-axis in the magnetic ground state and cancel each other at zero field[23]. A magnetic field larger than 0.2 T is necessary to polarize them. These issues are, however, absent in the superlattice structure, where the canted moments of different layers always maintain a parallel alignment and the interlayer coupling can be tuned and suppressed[18].

Monte Carlo simulation and fitting parameters. As derived in the main text, the crossover temperature is given by

$$T_0 = T_{\mathrm{BKT}} + \frac{4b^2 T_{\mathrm{BKT}}}{\left[\ln\left(\frac{\tilde{c}\tilde{J}S^2}{2 |J_\perp| S^2 + S |h\sin\varphi|} \right) \right]^2} \tag{5}$$

To estimate the parameter b, we performed the classical Monte Carlo simulation with up to $6{,}144 \times 6{,}144$ spins for the model

$$H = \sum_{\langle i,j \rangle} [\tilde{J}\tilde{\mathbf{S}}_i \cdot \tilde{\mathbf{S}}_j - \Gamma_1 \tilde{S}_i^z \tilde{S}_j^z \pm \Gamma_2 (\tilde{S}_i^x \tilde{S}_j^x - \tilde{S}_i^y \tilde{S}_j^y)] - h\cos\varphi \sum_i \tilde{S}_i^x$$
$$+ h\sin\varphi \sum_i e^{i\mathbf{Q} \cdot \mathbf{r}_i} \tilde{S}_i^y \tag{6}$$

where $+$ ($-$) is taken for bonds along the x(y)-axis, and $\mathbf{Q} = (\pi, \pi)$ is the antiferromagnetic ordering wavevector, and Γ_1 and Γ_2 terms are high-order corrections introduced by the Hund's coupling[19]. In the superlattice, the in-plane

rotation angle of octahedra is estimated[28] to be approximately 8°, which is slightly smaller than that of bulk Sr_2IrO_4. Accordingly, we set $\tan 2\varphi = D/J = 0.27$. For other parameters, we set $\Gamma_1 = 10^{-4}J$, corresponding to an out-of-plane gap $\Delta \sim 1$ meV (refs [42,43]), and $\Gamma_2 = 5\Gamma_1$ (ref. [19]). Because the Γ_2 term does not affect the energy of the canted-spin ground state in the classical spin limit, it is not expected to affect T_0. We confirmed that the dependence of the crossover temperature on Γ_2 is of order $\Gamma_2/\tilde{J}$ and negligible, therefore the Γ_2 term was omitted in the discussion of the main text. The magnetic field was set down to $h = 2 \times 10^{-5}J$, corresponding to a magnetic field ~ 0.01 T as applied in our experiments. The crossover temperature was calculated in the same way with the experimental results as the inflection point of the antiferromagnetic order parameter as a function of temperature, $\sqrt{|\widetilde{M}_{st}|^2}$, where $\widetilde{M}_{st} = \sum_i e^{i\mathbf{Q} \cdot \mathbf{r}_i} \widetilde{S}_i^y$.

Above the Berezinskii–Kosterlitz–Thouless transition temperature (T_{BKT}), the correlation length diverges as $\xi \sim e^{\frac{b}{\sqrt{t}}}$ (ref. [44]) where $t = \frac{T}{T_{BKT}} - 1$. In the SU(2) symmetric case, it diverges in the vicinity of zero temperature as $\xi \sim e^{\frac{2\rho_s}{T}}$ (ref. [14]), where ρ_s is the spin stiffness. These two expressions should be smoothly connected in the isotropic limit ($T_{BKT} \to 0$), which implies $b \to \infty$. Therefore, the closer to the SU(2) symmetry the interaction is, the faster the divergence of the correlation length becomes. These expressions for the correlation length are valid for both the quantum and the classical spins. Because the quantum nature is expected to be irrelevant with regard to ordering, the difference in the scaling of the correlation length between the quantum and the classical spins is only the renormalization of the energy—namely, the transition temperature or the spin stiffness. We thus expect the parameter b to be independent of the length of spins.

Fitting the numerically obtained data to equation (5), we estimated $T_{BKT}^{cl} \approx 210$ K and $b \approx 3.1$. We used $\tilde{J} \approx 500$ K, which is a common energy scale for magnetic iridates, especially layered systems[32]. Then we fitted the experimental data, fixing the value of b, and estimated $T_{BKT}^q \approx 18$ K and $J_\perp \approx 0.007$ K. In terms of the parameter c, which is proportional to the effective energy of vortices, namely the spin stiffness ($c \propto \rho_s$), we obtained $c^{cl} \sim 1$ for the classical spins and $c^q \sim 10^{-1}$ for the experimental data. Because $\rho_s \propto T_{BKT}$ at the Berezinskii–Kosterlitz–Thouless transition[45], our estimations are consistent: $c^q/c^{cl} \approx T_{BKT}^q/T_{BKT}^{cl} \sim 10^{-1}$. The reduction of the transition temperature can be explained by the quantum fluctuations and possible disorder in the real material.

Theoretical calculations on non-SU(2)-invariant exchange interaction models. To further check the crucial role of the SU(2)-invariant exchange, we have calculated the field-induced effect for different values of the exchange anisotropy. Specifically, we considered three different models. The first model is the one discussed in the manuscript, where the exchange anisotropy $\Gamma_1 = 10^{-4}J$ is included to take into account the smaller higher-order correction from Hund's coupling in the real material under consideration. The model remains quasi-SU(2)-invariant and is highly consistent with the experimental observation (Fig. 3a). The second model corresponds to a hypothetical situation where the symmetric anisotropic exchange is artificially removed ($\delta = 0$ in Eq. (1)), and the only source of anisotropy is the DM interaction. In this case, the exchange anisotropy is no longer SU(2)-invariant but has a relatively strong U(1) symmetry since the DM interaction alone favours an easy-plane anisotropy. In the third model, the easy-plane anisotropy is further increased to the XY-limit by setting $\Gamma_1 = \tilde{J}$.

For the second and third models, the constant b was estimated to be ~ 1.8 and ~ 1.4, respectively, from classical Monte Carlo calculations, consistent with a previous work[46]. By keeping the other parameters the same as those in the quasi-SU(2) model, we extracted the relative enhancement of T_0 as a function of the in-plane magnetic field in the two situations. As shown in Supplementary Fig. 6, both the second and the third models show a much weaker relative increase of T_0 in response to an external magnetic field as compared with the quasi-SU(2)-invariant case, and are not able to account for the observed effect. This is understandable because the constant b must increase upon approaching the SU(2)-invariant point in order to describe the crossover from the temperature dependence of the magnetic correlation length of a 2D U(1) magnet, $\xi \sim e^{b/\sqrt{t}}$, where $t = \frac{T - T_{BKT}}{T_{BKT}}$, to the behaviour characteristic of a SU(2) magnet: $\xi \propto e^{2\pi\rho_s/T}$.

Data Availability. The data that support the plots within this paper and other findings of this study are available from the corresponding author upon reasonable request.

References
34. Perdew, J. P., Burke, K. & Ernzerhof, M. Generalized Gradient Approximation made simple. *Phys. Rev. Lett.* **77**, 3865–3868 (1996).
35. Kresse, G. & Furthmüller, J. Efficient iterative schemes for ab initio total-energy calculations using a plane-wave basis set. *Phys. Rev. B* **54**, 11169–11186 (1996).
36. Zhang, L. et al. Oxygen vacancy diffusion in bulk $SrTiO_3$ from density functional theory calculations. *Comput. Mater. Sci.* **118**, 309–315 (2016).
37. Glazer, A. M. The classification of tilted octahedra in perovskites. *Acta Cryst. B* **B28**, 3384–3392 1972).
38. Glazer, A. M. Simple ways of determining perovskite structures. *Acta Cryst. A* **31**, 756–762 1975).
39. Brahlek, M., Choquette, A. K., Smith, C. R., Engel-Herbert, R. & May, S. J. Structural refinement of Pbnm-type perovskite films from analysis of half-order diffraction peaks. *J. Appl. Phys.* **121**, 045303 (2017).
40. Fujiyama, S. et al. Two-dimensional Heisenberg behavior of $J_{eff} = 1/2$ isospins in the paramagnetic state of the spin–orbital Mott insulator Sr_2IrO_4. *Phys. Rev. Lett.* **108**, 247212 (2012).
41. Takayama, T., Matsumoto, A., Jackeli, G. & Takagi, H. Model analysis of magnetic susceptibility of Sr_2IrO_4: A two-dimensional $J_{eff} = 1/2$ Heisenberg system with competing interlayer couplings. *Phys. Rev. B* **94**, 224420 (2016).
42. Bahr, S. et al. Low-energy magnetic excitations in the spin–orbital Mott insulator Sr_2IrO_4. *Phys. Rev. B* **89**, 180401 (2014).
43. Gim, Y. et al. Isotropic and anisotropic regimes of the field-dependent spin dynamics in Sr_2IrO_4: Raman scattering studies. *Phys. Rev. B* **93**, 024405 (2016).
44. Kosterlitz, J. M. The critical properties of the two-dimensional XY model. *J. Phys.* **C7**, 1046–1066 (1974).
45. Nelson, D. R. & Kosterlitz, J. M. Universal jump in the superfluid density of two-dimensional superfluids. *Phys. Rev. Lett.* **39**, 1201–1205 (1977).
46. Cuccoli, A., Tognetti, V. & Vaia, R. Two-dimensional XXZ model on a square lattice: A Monte Carlo simulation. *Phys. Rev. B* **52**, 10221–10231 (1995).